CRYSTALLOGRAPHY REPORTS, 2025, Vol. 70, No. 1, pp. 121–127

NANOMATERIALS, CERAMICS

INVESTIGATION OF PHOTONIC CURING MECHANISMS OF SOL-GEL ZINC OXIDE FILMS FOR FLEXIBLE ELECTRONICS

© 2025 I. A. Pronin[a], A. S. Komolov[b], E. F. Lazneva[b], V. A. Moshnikov[c], A. A. Karmanov[a,*], and N. D. Yakushova[a]

[a] Penza State University, Penza, Russia
[b] Saint Petersburg State University, Saint Petersburg, Russia
[c] Saint Petersburg Electrotechnical University, Saint Petersburg, Russia
*e-mail: starosta07km1@mail.ru

Received September 11, 2024
Revised September 17, 2024
Accepted September 17, 2024

Abstract. Photoannealing is a technological method that allows replacing the final high-temperature treatment of metal oxide sol-gel films with a combination of soft heating and ultraviolet irradiation. It has been established that an increase in temperature during heat treatment of the sol deposited on the substrate leads to the conversion of zinc acetate into layered basic zinc acetate (*LBZA*), which is transformed into hydroxide $Zn(OH)_2$, which passes into amorphous oxide ZnO. It is shown that when heated to 130°C, parallel irradiation of films with UV radiation promotes the direct transition of LBZA into oxide due to the effective removal of hydroxyl and acetate groups. When the temperature is increased to 140°C, UV irradiation of films loses its expediency, since both photoannealing and heat treatment lead to identical properties of the studied materials.

DOI: 10.31857/S00234761250117e1

INTRODUCTION

Semiconductor metal oxides (SMO) are a group of materials widely used in electronics. For example, tin oxide is the main material for the production of sensitive elements of chemoresistive gas sensors [1]; a solid solution of tin and indium oxides is a transparent conducting material used as an electrode in liquid crystal and touch screens [2]; thin films and nanostructures of zinc oxide are used to produce varistors [3], thin-film transparent transistors [4], and biosensors [5]. There are many methods for forming SMO film structures, including both physical (magnetron sputtering, thermal vacuum deposition) and chemical (e.g. sol-gel, spray pyrolysis) methods. An important feature of both groups of methods is the high-temperature (usually at 400°C and higher) effect on the substrate. In the group of vacuum methods, a stream of material is deposited onto a preheated substrate; In chemical methods for forming a semiconductor layer, finishing heat treatment is used, during which metal salts and hydroxides are converted into oxides. This significantly limits the use of POM in flexible and epidermal electronics, where thermoplastic substrates with low melting temperatures are used (e.g., polyethylene terephthalate, T_m ~ 260°C [6]; polyethylene naphthalate, T_m ~ 280°C [7]). In this regard, the approach first proposed in 2012 [8], which consists of transforming sol-gel films into semiconductor oxides under the influence of UV radiation with relatively low additional heating (today, the terms "photoannealing" and "photonic curing" are used in the literature), is of great interest for flexible electronics. This technology in its various modifications is used to manufacture flexible thin-film transistors [9, 10], gas sensors [11, 12], solar cells [13, 14], and flexible quantum dot LEDs [15]. However, fundamental physical and chemical concepts of the formation of oxide layers during photonic curing are currently lacking [16]. It has only been proven that photoannealing allows for the formation of a denser metal oxide network, the effective removal of organic impurities, and the improvement of electrical conductivity [17]. It is known that the energy of ultraviolet photons is sufficient to break chemical bonds in sol-gel systems, and numerical modeling shows a decrease in curing temperatures with combined UV and thermal treatment of films [18]. However, the contribution of thermal and photochemical processes to the final result is difficult to differentiate, since photoannealing processes occur simultaneously and inseparably from each other. The data available in the literature only allow us to say that the films obtained by classical high-temperature annealing and photoannealing are practically identical. For example, in [8] practically identical phase and chemical compositions of films of a solid solution of zinc, gallium and indium oxides obtained by the classical sol-gel method at an annealing temperature of 350°C and photoannealing with additional heating to 150°C are shown. Data from studies of physicochemical processes in the intermediate temperature range are not presented.

In this work, the problem of differentiation of thermo- and photochemical contributions to the processes of curing and formation of a semiconductor of sol-gel films based on zinc oxide is solved for the first time. For this purpose, on the basis of an array of experimental data, the specific energy of UV radiation of the treatment is selected, which allows providing a semiconductor type of absorption of optical radiation by the obtained films in a narrow temperature range with separately taken combined (UV + thermal) and thermal treatments.

METHODS AND MATERIALS

The following procedure was used to prepare the sol. In the first step, zinc acetate dihydrate was dissolved in a mixture of 2-methoxyethanol and 2-aminoethanol (all reagents from Sigma-Aldrich®, Saint Louis, MO, USA) for 15 min at room temperature. The sol was then stirred for 1 h at 60°C and matured for 24 h at room temperature (~25°C). The sol was applied to silicon (KEF15) and quartz (KU-1) substrates by centrifugation at 3000 rpm for 60 s, followed by drying at 90°C for 1 h in air. The samples were subjected to two types of finishing: thermal and combined (ultraviolet + thermal). Thermal treatment was carried out at temperatures of 120, 130 and 140°C (samples 120(T), 130(T) and 140(T), respectively) on a PL-01 laboratory hotplate (OOO NPP TOMANALIT, Russia) for 90 min. Combined treatment was carried out at the same temperatures; additionally, the film was irradiated with an 8 W linear UV lamp with radiation maxima at 185 and 254 nm (WL 2001, lamp type T5 G5, Camelion, China) (samples 120(T+UV), 130(T+UV) and 140(T+UV)); the distance from the lamp to the film surface was 20 mm.

The phase composition of the samples was studied on a D8 Discover X-ray diffractometer (Bruker) with a CuK_α radiation source ($\lambda = 0.15406$ nm) in the 2θ range of 4°–64°.

The surface chemical composition of the obtained samples was analyzed by X-ray photoelectron spectroscopy (**XPS**). The XPS spectra were measured under ultrahigh vacuum (10^{-7} Pa) using an Escalab 250Xi spectrometer (Thermo Fisher Scientific Inc., Waltham, MA, USA) with a photon energy of AlK_α = 1486 eV. The XPS peaks were deconvoluted by subtracting the Shirley background followed by peak fitting with the Voigt function. To remove surface contamination associated with atmospheric adsorbates, the surface of the films was gently etched with Ar^+ ions at a current of 1 μA for 30 s. The energy scale of the spectrometer was calibrated using a sputter-cleaned Au surface as a reference, so that the binding energy of the Au4$f_{7/2}$ peak was set to 84.0 eV.

The absorption spectra of all samples on a quartz substrate were recorded in the range of 190–1100 nm using an SF-56 spectrophotometer (LOMO JSC, Russia) and reconstructed in Tautz coordinates [19].

DISCUSSION OF RESULTS

Figure 1 shows the diffraction patterns of all sample series. Three reflections 001, 002 and 003 at $2\theta = 6.0°$, 12.2° and 18.2°, respectively, can be clearly identified in the diffraction pattern of sample 120(T). These reflections correspond to layered basic zinc acetate (Layered Basic Zinc Acetate – **LBZA**, $Zn_5(CH_3COO)_8(OH)_2 \cdot 2H_2O$) [20]. LBZA is an intermediate product of the conversion of zinc acetate to oxide in solutions. During the maturation of the sol, the acetate groups are replaced by OH groups, and the entire scheme of transformations in ZnO is usually presented in a simplified form [21]:

$$Zn(CH_3COO)_2 \cdot 2H_2O \rightarrow \text{LBZA} \rightarrow Zn(OH)_2 \rightarrow ZnO.$$

The crystal structure of LBZA is shown in the inset of Fig. 1. In it, three of the five zinc cations are surrounded by six hydroxyl groups in an octahedral configuration. The two remaining zinc cations are located above and below an empty octahedron at the center of the tetrahedron, the vertices of which are two hydroxyl groups and one water molecule. Acetate ions are intercalated between the layers. The transformation of LBZA to ZnO occurs by sequential removal of water molecules (~70°C), hydroxyl groups (~120°C), and acetate ions (~130–350°C) [22].

The interlayer distance in LBZA for sample 120(T), calculated using the Wulff–Bragg equation, is 1.47 nm. Calculation of the average sizes of coherent scattering regions (**CSR**) of the sample using the Scherrer equation [23] yielded a value of $D_{LBZA} = 8.5$ nm (Table 1), which allows us to speak about an average number of five to six layers in one nanoparticle.

Combined treatment at 120°C (sample 120(T+UV)) does not result in the appearance of new reflections, but in their significant broadening compared to sample 120(T): amorphization of the LBZA phase occurs, and the CSR size decreases to 5.8 nm, which corresponds on average to four layers in one nanoparticle. The diffraction pattern of sample 130(T) contains only a strongly broadened (full width at half maximum 2.04°) reflection 001 LZBA. The calculated average CSR size was 3.9 nm (corresponds to two to three layers). All other samples (130(T+UV), 140(T), 140(T+UV)) turned out to be X-ray amorphous, and the diffraction patterns did not contain reflections of any phases, which indicates the transformation of LZBA into other chemical compounds.

Fig. 2 shows the absorption spectra of all the studied samples in the UV and visible ranges of the spectrum, reconstructed in the Tauc coordinates $((\alpha E)^2 = f(E)$, where α is the absorption coefficient [1/cm], E is the photon energy [eV]). Films 120(T), 120(T+UV) and 130(T) do not demonstrate interband absorption, typical of semiconductors at a photon energy equal to and exceeding the band gap, and are practically transparent to photons with energies less than 4 eV. Sample

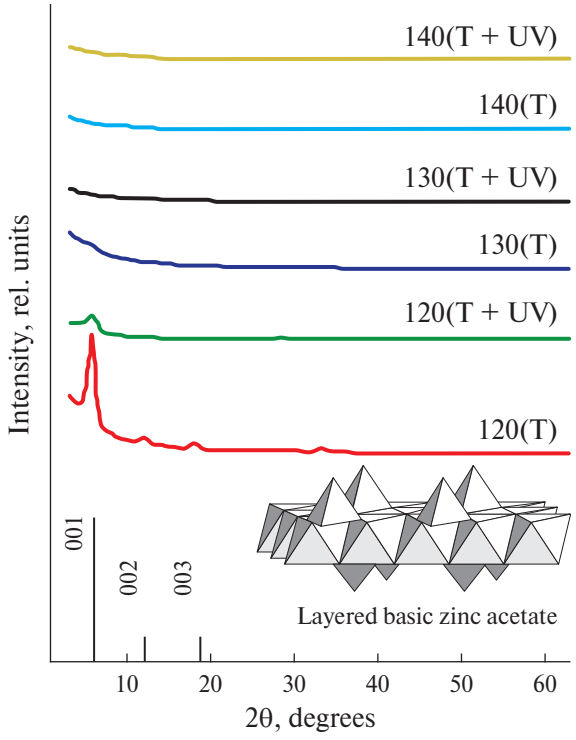

Fig. 1. Diffraction patterns of zinc oxide sol-gel film samples. The inset shows the crystalline structure of LBZA.

130(T+UV) demonstrates an optical gap corresponding to a direct-band semiconductor material, since a straight-line section appears in the chosen coordinates. Its extrapolation to the intersection with the abscissa axis yields the width of the optical gap, which for this sample is $\Delta E_g = 3.32$ eV, which corresponds to the formation of zinc oxide [24]. Finally, samples 140(T) and 140(T+UV) exhibit almost identical spectra, corresponding to a semiconductor material with $\Delta E_g = 3.27$ eV.

It is important to note that the formation of X-ray amorphous semiconductor films occurs only when the LBZA phase reflections disappear from the diffraction patterns. Temperature treatment at 130°C alone does not initiate this process, but its combination with UV irradiation, on the contrary, forms ZnO. To understand the physicochemical processes occurring in the films, let us consider the XPS spectra. XPS shows that the samples contain zinc, oxygen, and carbon.

Fig. 3 shows the spectra of Zn2*p* and O1*s*. The Zn2*p* spectrum is represented by a doublet of $Zn2p_{1/2}$ and $Zn2p_{3/2}$. For further analysis, it is sufficient to restrict ourselves to the $Zn2p_{3/2}$ component. Its binding energy is in the range of 1021.15–1022.1 eV. These values can correspond to both the zinc cation Zn^{2+} in the ZnO lattice [25, 26] and zinc in the hydroxide $Zn(OH)_2$ [27] and LBZA [28]. Due to this, it is difficult to use this spectrum to differentiate the forms of zinc in the material. Deconvolution of the O1*s* spectrum makes it possible to isolate two components with binding energies of about 530.3 and 532.0 eV. The first, O(lat), corresponds to the Zn–O bond in zinc oxide, and the second, O(ads), to the Zn–OH bonds in the hydroxide and LBZA [29]. Deconvolution of the C1*s* spectrum (Fig. 4) shows the existence of three forms of carbon in the films: C_{-C-C-}, C_{C-H} and $C_{C=O}$ with a binding energy of about 285.0, 286.5 and 290.0 eV, respectively. The first form corresponds to the existence of carbon on the surface in the form of graphite. The second refers to fragments of functional groups of organic compounds $-CH_3$, $-CH_2$, $-CH$. The third corresponds to the carbonyl group C=O. The $C_{C=O}$ form of all the precursors and intermediate compounds is contained only in acetate groups, which are intercalated between the LBZA layers.

Analysis of the spectra in Fig. 4 shows that samples 120(T) and 120(T+UV) contain a significant proportion of carbon atoms included in the carbonyl group (34 and 27 % of the total carbon in the films, respectively). However, already in sample 130(T) its significant reduction and accumulation of carbon on the surface in the form of C_{-C-C-} are observed. Probably, this is due to the removal of acetate ions from the film and their transformation into amorphous carbon (soot). Table 1 also presents the

Table 1. Sample parameters

Sample	D_{LBZA}, nm	ΔE_g, eV	$\frac{[C_{C=O}]}{[Zn]}$	$\frac{[O(lat)]}{[O]}$	$\frac{[Zn(lat)]}{[Zn]}$
120(T)	8.5		0.18	0.30	0.29
120(T+UV)	5.8		0.10	0.50	0.39
130(T)	3.9		0.07	0.50	0.41
130(T+UV)		3.32	0.05	0.65	0.44
140(T)		3.27	0.05	0.63	0.45
140(T+UV)		3.27	0.05	0.65	0.45

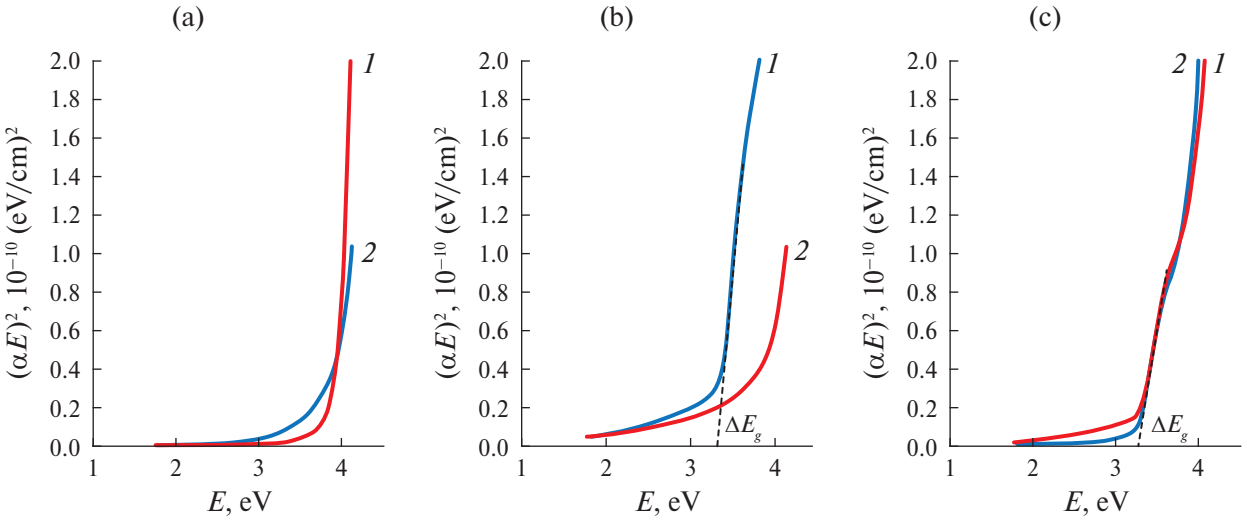

Fig. 2. Absorption spectra of samples in Tautz coordinates after thermal (*1*) and combined (*2*) treatment at a temperature of 120 (a), 130 (b) and 140°C (c).

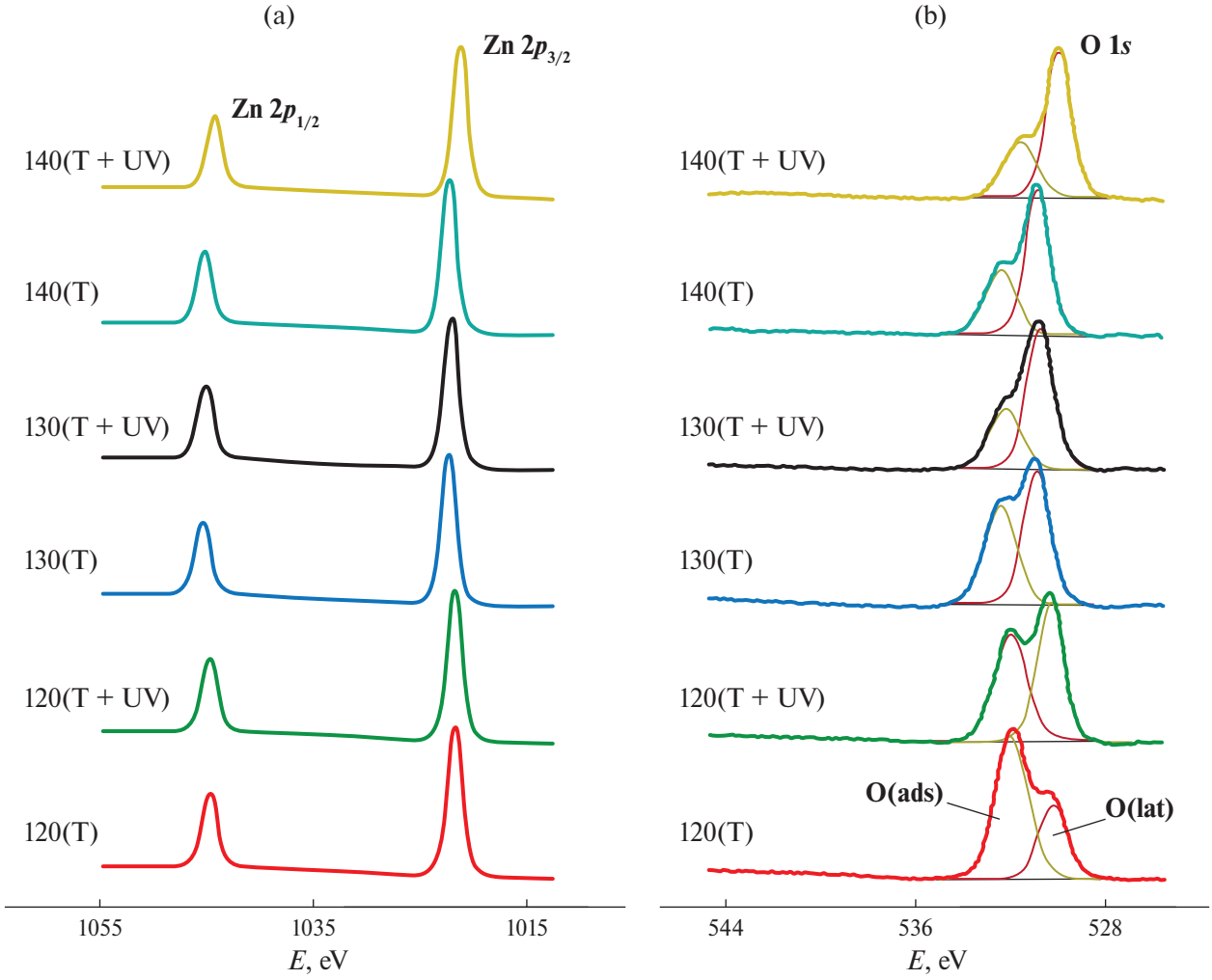

Fig. 3. XPS spectra of Zn2*p* (a) and O1*s* (b) samples.

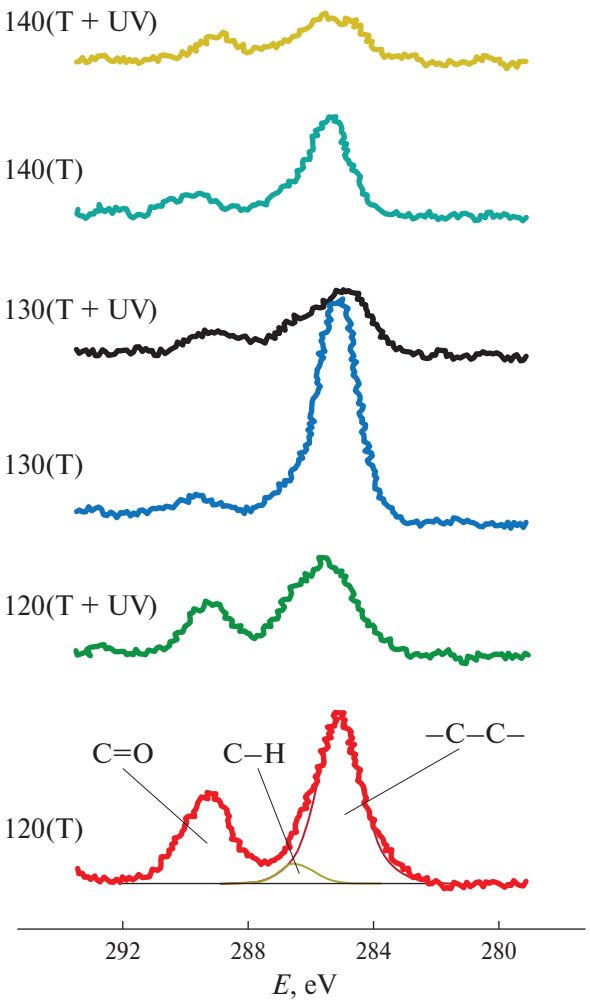

Fig. 4. XPS spectrum of C1*s* samples.

parameter $\frac{[C_{C=O}]}{[Zn]}$. For samples 130(T+UV), 140(T) and 140(T+UV) its value is only 5 %, which indicates almost complete removal of acetate groups from the film. This fact correlates with the disappearance of the LBZA phase reflections in the diffraction patterns of the same samples and the appearance of interband optical absorption characteristic of a direct-band semiconductor. Thus, it can be concluded that films 130(T+UV), 140(T) and 140(T+UV) represent a system of amorphous zinc oxide and hydroxide with different phase ratios.

Thus, to remove almost all acetate groups intercalated between the LBZA layers, heating the system to 130°C is sufficient, and the addition of UV radiation enhances this process (at 120°C, the $\frac{[C_{C=O}]}{[Zn]}$ ratio decreases from 0.18 to 0.10 when switching from thermal to combined annealing).

To estimate the ratio of amorphous phases of zinc oxide and hydroxide, we will consider the change in the ratio of the O(lat) and O(ads) forms under different treatment conditions. Table 1 shows the parameter $\frac{[O(lat)]}{[O]}$, which characterizes the proportion of oxygen in the sample occupying a position in the ZnO lattice. With an increase in the annealing temperature from 120 to 140°C, it increases from 0.3 to 0.63. Combined treatment under the same conditions demonstrates a contribution dependent on temperature: at 120°C it increases the proportion of $\frac{[O(lat)]}{[O]}$ from 30 to 50 %, at 130°C – from 50 to 65 %, at 140°C it shows virtually no difference from simple heat treatment. Based on the $\frac{Zn}{O} = 1:1$ ratio in pure ZnO, knowing the O(lat) value, it is possible to calculate the proportion of zinc cations included in the oxide nanocrystals: Table 1 shows the $\frac{[Zn(lat)]}{[Zn]}$ ratio. It is evident that at an annealing temperature of 120°C, 29 % of zinc cations are included in the Zn–O–Zn bonds in the particles. Nevertheless, the size of these particles is small, due to which there are no reflections of the ZnO phase in the diffraction pattern, and the films do not demonstrate semiconductor optical properties. Combined treatment at the same temperature makes it possible to increase the $\frac{[Zn(lat)]}{[Zn]}$ proportion to 39 %. At 130°C, the combined treatment increases the $\frac{[Zn(lat)]}{[Zn]}$ share from 41 to 44 % compared to heat treatment alone, and the sample acquires semiconductor properties and an optical gap of 3.32 eV. Finally, at 140°C, the combined treatment has no effect on the ratio: $\frac{[Zn(lat)]}{[Zn]} = 0.45$ in both cases, and the absorption spectra are semiconductor in nature and are virtually identical.

A combined analysis of XPS data, phase composition and optical absorption spectra reveals the following patterns. Combined photoannealing of films with the LBZA phase composition allows for a more intensive removal of intercalated acetate ions and hydroxyl groups from the sample compared to thermal action at the same temperature. However, after LBZA decomposition, both thermal and combined treatments at the same temperature lead to the same ratio of amorphous phases of ZnO and $Zn(OH)_2$, i.e. additional UV action during annealing becomes ineffective. In this regard, the final photoannealing operation of ZnO sol-gel films is most effective in removing hydroxyl groups from LBZA located at the vertices of the tetrahedron and octahedron, the center of which is zinc cations in the layered structure of this material. Then the differences

$$Zn(CH_3COO)_2 \rightarrow LBZA \begin{array}{l} \xrightarrow{\text{thermal annealing}} Zn(OH)_2 \rightarrow ZnO \\ \xrightarrow{\text{photo annealing}} ZnO \end{array}$$

between thermal annealing and photoannealing can be represented by the following scheme:

The combined treatment allows direct transformation of LBZA into ZnO (as observed in sample 130(T+UV)), but is ineffective in the Zn(OH)2 → ZnO transition.

CONCLUSION

The mechanisms of photonic curing of zinc oxide sol-gel films during photoannealing were studied. The conditions were experimentally selected that made it possible to obtain amorphous semiconductor ZnO films demonstrating an optical gap in the absorption spectrum using both mild thermal action and combined action in a narrow temperature range. For the selected conditions, the range was 120–140°C. At 120°C, neither combined nor thermal treatments resulted in the semiconductor type of radiation absorption. At 130°C, only photoannealing made it possible to obtain a film with a band gap of 3.32 eV. Treatment at 140°C (both combined and thermal) made it possible to form semiconductor films with $\Delta E_g = 3.27$ eV, spectrophotometrically indistinguishable from each other. The classical sol-gel process with final thermal annealing involves the conversion of zinc acetate into layered basic zinc acetate, which is transformed into hydroxide and finally into ZnO at high temperatures. Irradiation of films during heat treatment at low temperatures with UV radiation allows for the effective removal of acetate and hydroxyl groups and the formation of amorphous zinc oxide films. It has been shown that these processes occur only in layered basic zinc acetate. After its thermal transformation into $Zn(OH)_2$ at a higher temperature, the effectiveness of combined annealing for further transition to ZnO disappears.

FUNDING

The study was supported by the grant of the Russian Science Foundation No. 23-29-00844, https://rscf.ru/project/23-29-00844/. The experiments were carried out using the equipment of the Research Park of St. Petersburg State University, “Physical methods of surface investigation”, “Centre for X-ray Diffraction Studies”.

CONFLICT OF INTERESTS

The authors of this work declare that they have no conflicts of interest.

REFERENCES

1. *Korotcenkov G., Brinzari V., Schwank J. et al.* // Sens. Actuators. B. 2001. V. 77. No. 1–2. P. 244. https://doi.org/10.1016/S0925-4005(01)00741-9
2. *Waldman L.J., Haunert D.P., Carson J.D. et al.* // ACS Omega. 2024. V. 9. No. 27. P. 29732. https://doi.org/10.1021/acsomega.4c03288
3. *Ren X., Yang L., Cheng Q. et al.* // J. Mater. Sci.: Mater. Electron. 2024. V. 35. No. 3. P. 217. https://doi.org/10.1007/s10854-024-11949-2
4. *Kumar B.B., Tiwari P.K., Dubey S. et al.* // Micro Nanostructures. 2022. V. 164. P. 107122. https://doi.org/10.1016/j.spmi.2021.107122
5. *Krishna M.S., Singh S., Batool M. et al.* // Mater. Adv. 2023. V. 4. No. 2. P. 320. https://doi.org/10.1039/D2MA00878E
6. *Yakimets I., MacKerron D., Giesen P. et al.* // Adv. Mater. Res. 2010. V. 93. P. 5. https://doi.org/10.4028/www.scientific.net/AMR.93-94.5
7. *Lamanna L., Rizzi F., Guido F. et al.* // Adv. Electron. Mater. 2019. V. 5. No. 6. P. 1900095. https://doi.org/10.1002/aelm.201900095
8. *Kim Y.-H., Heo J.-S., Kim T.-H. et al.* // Nature. 2012. V. 489. P. 128. https://doi.org/10.1038/nature11434
9. *Park J.W., Kang B.H., Kim H.J.* // Adv. Funct. Mater. 2020. V. 30. No. 20. P. 1904632. https://doi.org/10.1002/adfm.201904632
10. *Leppaniemi J., Eiroma K., Majumdar H. et al.* // ACS Appl. Mater. Interfaces. 2017. V. 9. No. 10. P. 8774. https://doi.org/10.1021/acsami.6b14654
11. *Pronin I.A., Plugin I.A., Kolosov D.A. et al.* // Sens. Actuators. A. 2024. V. 377. P. 115707. https://doi.org/10.1016/j.sna.2024.115707
12. *Jaisutti R., Kim J., Park S.K. et al.* // ACS Appl. Mater. Interfaces. 2016. V. 8. No. 31. P. 20192. https://doi.org/10.1021/acsami.6b05724
13. *Dong Z., Wang J., Men J. et al.* // Inorg. Chem. 2024. V. 63. No. 12. P. 5709. https://doi.org/10.1021/acs.inorgchem.4c00178
14. *Subbiah A.S., Mathews N., Mhaisalkar S. et al.* // ACS En. Lett. 2018. V. 3. No. 7. P. 1482. https://doi.org/10.1021/acsenergylett.8b00692
15. *Lima A.H., Raeyani D., Sudmand S.A. et al.* // Opt. Mater. 2024. V. 149. P. 115041. https://doi.org/10.1016/j.optmat.2024.115041
16. *Hsu J.W., Piper R.T.* // J. Phys. D. 2024. V. 57. No. 25. P. 252001. https://doi.org/10.1088/1361-6463/ad3560

17. *John R.A., Chien N.A., Shukla S.et al.* // Chem. Mater. 2016. V. 28. No. 22. P. 8305. https://doi.org/10.1021/acs.chemmater.6b03499
18. *Piper R.T., Xu W., Hsu J.W.* // IEEE J. Photovolt. 2022. V. 12. No. 3. P. 722. https://doi.org/10.1109/JPHOTOV.2022.3159395
19. *Tauc J.* Amorphous and Liquid Semiconductors. Springer Science and Business Media, 2012. 441 p. https://doi.org/10.1007/978-1-4615-8705-7
20. *Song R.Q., Xu A.W., Deng B. et al.* // Adv. Funct. Mater. 2007. V. 17. No. 2. P. 296. https://doi.org/10.1002/adfm.200600024
21. *Wang Y., Li Y., Zhou Z. et al.* // J. Nanoparticle Res. 2011. V. 13. P. 5193. https://doi.org/10.1007/s11051-011-0504-y
22. *Hosono E., Fujihara S., Kimura T. et al.* // J. Colloid Interface Sci. 2004. V. 272. No. 2. P. 391. https://doi.org/10.1016/j.jcis.2003.10.005
23. *Holzwarth U., Gibson N.* // Nature Nanotechnol. 2011. V. 6. No. 9. P. 534. https://doi.org/10.1038/nnano.2011.145
24. *Coleman V.A., Jagadish C.* // Zinc Oxide Bulk, Thin Films and Nanostructures. Elsevier Science Ltd, 2006. P. 1. https://doi.org/10.1016/B978-008044722-3/50001-4
25. *Pronin I.A., Averin I.A., Karmanov A.A et al.* // Nanomaterials. 2022. V. 12. No. 11. P. 1924. https://doi.org/10.3390/nano12111924
26. *Filippov I.A., Karmanov A.A., Yakushova N.D.* et al. //Crystallography Reports. 2024. V. 69. No. 7. P. 1162. https://doi.org/10.1134/S106377452460162X
27. *Duchoslav J., Steinberger R., Arndt M. et al.* // Corrosion Sci. 2014. V. 82. P. 356. https://doi.org/10.1016/j.corsci.2014.01.037
28. *Liang M.K., Limo M.J., Sola-Rabada A. et al.* // Chem. Mater. 2014. V. 26. No. 14. P. 4119. https://doi.org/10.1021/cm501096p
29. *Frankcombe T.J., Liu Y.* // Chem. Mater. 2023. V. 35. No. 14. P. 5468. https://doi.org/10.1021/acs.chemmater.3c00801